Effect of bainitic or martensitic microstructure of a pressure vessel steel on grain boundary segregation induced by step cooling simulating thermal aging

Chih-Ying Hsu, J. Stodolna, P. Todeschini, F. Delabrouille, Frédéric Christien

Effect of Bainitic or Martensitic Microstructure of a Pressure Vessel Steel on Grain Boundary Segregation Induced by Step Cooling Simulating Thermal Aging

C.-Y. Hsu[1,2*], J. Stodolna[1], P. Todeschini[1], F. Delabrouille[1], F. Christien[2]

1: EDF R&D, MMC Department, F-77250 Ecuelles, France

2: Mines Saint-Etienne, Univ Lyon, CMRS, UMR 5307 LGF, Centre SMS, F-42023 Saint-Etienne, France

---

Keywords: Phosphorus, 16MND5, SA508, low alloy steel, STEM-EDX, intergranular segregation, bainite, martensite, reactor pressure vessel steel, thermal aging, reversible temper embrittlement, step cooling

Abstract

During operating lifetime of a nuclear power plant, the pressure boundary components, usually in 16MND5 (SA508 Cl. 3) steel, are subjected to thermal aging that may induce phosphorus intergranular segregation. This is known to decrease brittle fracture stress and induce intergranular fracture, which causes reversible temper embrittlement. Large components such as the reactor pressure vessel presents microstructure heterogeneity due to forging and welding. Tempered martensite can locally be found in the nominally bainitic steel. The question of microstructure susceptibility to reversible temper embrittlement has been raised in literature suggesting that tempered martensite has higher sensibility to phosphorus intergranular segregation than tempered bainite. In this paper, a comparative study of intergranular segregation in tempered bainitic and martensitic 16MND5 steel after thermal aging is conducted using energy dispersive X-ray spectroscopy on transmission electron microscope. Focus ion beam is used to precisely prepare lamellae at prior austenite grain boundaries on step cooled bainitic and martensitic samples. Different types of grain boundaries are identified using

precession assisted crystal orientation mapping and then the local chemical composition is analyzed. Phosphorus, nickel, manganese and molybdenum were observed at all types of grain boundaries in both microstructures. The segregation levels are higher in prior austenitic grain boundaries than in other types of boundaries for both microstructures. Taking into account the segregation amount in different types of boundaries, the phosphorus bulk depletion is shown negligible. The results show similar segregation levels in the two studied microstructures, indicating that the susceptibility to thermally induced grain boundary segregation between the tempered bainite and tempered martensite is the same.

1. Introduction

Thermal aging in nuclear power plants is due to long life time (> 40 years) operation at relatively low temperatures (290°C - 325°C, up to 345°C locally in the pressurizer). The degradation of material due to thermal aging is manifested by the decrease of fracture toughness and the increase of the Ductile-to-Brittle Transition Temperature (DBTT). One characteristic of thermal aging is a change of fracture mode from transgranular cleavage to intergranular fracture; the term “intergranular” here applies to the Prior Austenite Grain Boundaries (PAGBs). This phenomenon is known as Reversible Temper Embrittlement (RTE), which is a non-hardening mechanism due to the embrittlement of grain boundaries by segregation of impurities, notably phosphorus [1]–[5]. Intergranular segregation describes the local rearrangements of solute atoms at grain boundaries. This phenomenon can strongly affect the cohesive energy of the grain boundary, and thus the material properties. 16MND5 steel (similar to SA 508 Class 3) is widely used in the nuclear industry for the main pressure boundary components of the primary circuit of pressurized water reactors. The microstructure of these different components is nominally upper bainite [6]–[9]. However, martensite can be obtained in heat affected zones of

welds or claddings, in particular near the fusion line or in mesosegregations. Evidences of phosphorus intergranular segregation were confirmed in both western and eastern reactor pressure vessel steels [8], [10]–[14]. Miller *et al.* [14] mentioned that phosphorus intergranular segregation coverage in A533B steels after stress relieving heat treatment at 620°C, whose phosphorus bulk content is 110 wt ppm, is about 5% before service and 7% after 30 years of thermal aging at 290°C.

There are different studies [2]–[5], [10], [15]–[23] that have shown how phosphorus intergranular segregation is related to the mechanical property degradation. Druce *et al.* [4] showed that in coarse grain A533B steel, the change in DBTT is proportional to the P/Fe peak height ratio measured by Auger Electron Spectroscopy (AES). More studies [15], [16], [19] have also confirmed that phosphorus intergranular segregation has a direct link to the DBTT shift after aging. Boasen *et al.* [3] observed intergranular fracture on both A533B reference (80 wt ppm P) and weld metal (130 wt ppm P) after thermal aging. Erhart *et al.* [17] showed that intergranular fracture percentage increases when phosphorus grain boundary segregation increases. Nakata *et al.* [2] showed that the phosphorus peak height ratio is proportional to DBTT shift and intergranular fracture percentage. Similar effect was observed by Naudin *et al.* [5] on a model steel that has a composition similar to that of A-segregates (ghost lines). Those authors also observed that when the phosphorus monolayer coverage increases, the critical fracture stress decreases. Takayama *et al.* [18] have proposed an equation to elaborate the relationship between DBTT shift and phosphorus intergranular segregation. Their equation highlights the synergetic effect between hardness and segregation then further includes the influence of grain size. These different factors have also been confirmed by others in different steels [10], [20]–[23].

Literature [4], [5], [8], [11], [24]–[27] has raised the discussion of the microstructure susceptibility to RTE. The observations of different RTE behaviors between the base metal (upper bainite) and the heat affected zone (bainite and martensite) in several studies have led to the assumption of distinct phosphorus intergranular segregation behaviors between the martensitic and bainitic microstructure. Viswanathan and Joshi [27] worked on Cr-Mo-V steel (250 wt ppm P) and found that after the same tempering time, the phosphorus peak height ratio by AES is higher in martensite than in bainite. They also showed that at comparable ΔFATT (Fracture Appearance Transition Temperature shift), martensitic microstructure presents higher intergranular fracture percentage than bainitic microstructure. The same conclusion is confirmed by other studies [8], [11], [24], [25].

To measure intergranular segregation, the most common technique used is AES [12]. AES requires fresh intergranular fracture surfaces obtained under ultra-high vacuum. Its drawback is the impossibility to measure non-embrittled grain boundaries. Other techniques such as atom probe tomography [28]–[30] and Energy Dispersive X-ray Spectroscopy (EDX) on Transmission Electron Microscope (TEM) [31]–[37] were also used to measure grain boundary segregation as these techniques provide the possibility to analyze any grain boundary thanks to the development of Focus Ion Beam (FIB). The authors of this paper have recently developed a quantitative method for the measurements of grain boundary segregation by EDX using the Scanning mode on a Transmission Electron Microscope (STEM-EDX) [38], [39].

There are different factors that can influence the phosphorus segregation behavior, such as the bulk phosphorus content [2], [16], [17], [40], grain size [11], [41], and interactions with other alloying element [17], [42]–[46]. In general, phosphorus intergranular segregation prefers High Angle Grain Boundaries (HAGBs) and Σ3 boundaries have zero or very low segregation level [30],

[34], [47], [48]. The martensitic transformation breaks down the austenite grains into different sub-grains during phase transformation, which results in packet, block, and lath boundaries. The morphology of lath martensite in steels was well described in [49], [50]. Although the morphology of bainite can be more complicated to define as described by different authors [51]–[54], the same grain boundary categorization as for martensite can still be applied for bainitic grain boundaries since the phase transformation from the austenite parent phase follows certain orientation relationships [15], [55], [56]. Gourgues *et al.* [56] studied a A533B steel with martensite and upper bainite structures using Electron Backscatter Diffraction (EBSD) and suggested that upper bainite has highly misoriented packet boundaries (misorientations between 47° - 60°) that are not twin related and that martensite has a high population of Σ3 boundaries. Due to the nature of AES measurements – that inherently require a grain boundary to have been sufficiently embrittled such that intergranular fracture can be induced – PAGBs are the most analyzed among other types of grain boundaries. Apart from PAGBs, very few measurements were performed on other grain boundaries. Miller *et al.* [14] have discovered phosphorus intergranular segregation in lath boundaries by atom probe field ion microscopy. Doig *et al.* [57] also suggested that there are amounts of "alloying elements" segregated at bainite lath boundaries, but the amount is four times smaller than at PAGBs. Zhang *et al.* [30] analyzed 16MND5 weld and showed phosphorus segregation at all sorts of grain boundaries.

To further elaborate the different intergranular segregation behaviors in bainite and martensite, a hypothesis is proposed in the literature. Raoul *et al.* [11] showed that martensitic microstructure is more sensitive to intergranular fracture than bainitic microstructure for A533B steel. They suggested that this is because bainite has non PAGBs that can trap phosphorus and prevent it from segregating to PAGBs. Reversely, non PAGBs in martensite would trap less phosphorus, leaving more phosphorus free to segregate at PAGBs. In other words, the trapping

effect of phosphorus in bainite would be more important than in martensite, so that martensite would be more sensitive to thermal aging. Park *et al.* [8], partially confirmed the reasoning of Raoul *et al.* [11]. They showed that under the same thermal treatment, phosphorus concentration at PAGBs is higher in martensite (10.7%) than in bainite (7.1%). However, their AES results are given without details of peak height ratio interpretation. Also, they performed picric acid etching on bainitic and martensitic A508 Gr. 4N Ni-Cr-Mo steels, showing that phosphorus segregation appears also at packet boundaries in fully bainitic microstructure. They suggested that bainitic packet boundaries often have high misorientation, while high misoriented martensitic grain boundaries are often Σ3 boundaries. In other words, bainitic microstructure has more grain boundaries where phosphorus segregates than martensitic microstructure. Their assumption agrees with the study of Gourgues *et al.* [56] on the categorization of bainitic and martensitic grain boundaries.

The objective of this work is to understand the microstructure susceptibility to intergranular segregation induced by thermal aging. To achieve this, upper bainitic and martensitic low alloy steel samples were prepared. Step cooling heat treatment was performed to simulate thermal aging and induce phosphorus intergranular segregation. Microstructural studies were conducted using chemical etching and EBSD. FIB thin foils were prepared to precisely target PAGBs and other grain boundaries in the samples. Then the different types of grain boundaries in bainite and in martensite were identified using Precession Assisted Crystal Orientation Mapping (PACOM) in the TEM. The local composition at different types of grain boundaries was quantified using STEM-EDX. The quantification method was based on the box method proposed by the authors in a previous study [38]. The effect of microstructure on intergranular segregation is determined based on the results of STEM-EDX measurements conducted on 132 different grain boundaries.

2. Methodology

The material used in this study is a 16MND5 steel (similar to SA 508 Class 3) sampled in a heavy section forged shell in the quenched and tempered state (tempering at 645°C for about 7h). The measured chemical composition is listed in Table 1, with the phosphorus concentration of 0.008 wt%. Note that the chemical composition of the studied material complies with the French RCC-M standard.

Table 1 – Chemical composition of the studied material in weight percent.

C	Mn	Si	S	P	Ni	Cr	Mo	Cu	V	Al	Co	Ti
0.15	1.33	0.22	0.007	0.008	0.69	0.20	0.52	0.06	<0.005	0.03	0.02	0.004

The upper bainitic sample in this study was the original microstructure of the studied material, also referred to as the base metal. The martensitic sample (15 mm thickness) was created from the base metal that underwent austenitization at 900°C for an hour followed by water quench (cooling rate > 100°C/s at the center). This ensured a simple martensitic microstructure configuration to represent the heat affected zone to facilitate this study. The samples underwent a typical tempering process at 645°C for 6h45. To induce intergranular segregation, an accelerated step cooling cycle similar to the one in [11], [58] was applied on both samples. Figure 1 shows the step cooling cycle. One step cooled bainitic sample named as “bainite step cooling” (BSC) and one step cooled martensitic sample named as “martensite step cooling” (MSC) were prepared for STEM-EDX intergranular segregation analyses.

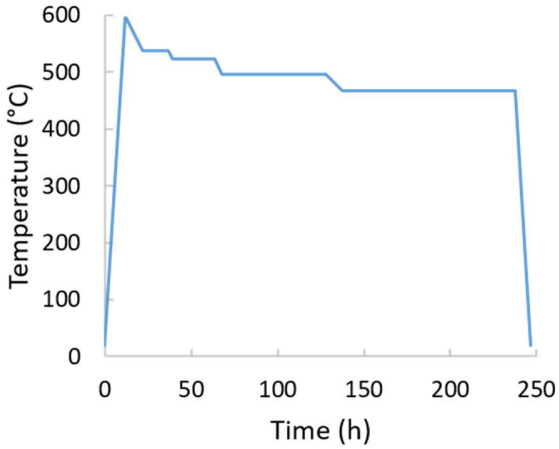

Figure 1: Step cooling cycle used for aging treatment.

Optical microscope and EBSD were used to investigate the studied microstructures. The as-quenched martensite sample and the two step cooled samples (BSC & MSC) were etched in nitric acid to reveal the microstructures and the carbides for optical microscope examination. Then the two samples were polished until colloidal silica, cleaned by water jet and ethanol ultrasound bath for EBSD acquisitions. The EBSD acquisitions were performed using a CMOS OXFORD SYMMETRY detector on Zeiss Supra 55 SEM for the bainitic sample and using a NORDIF UF1100 detector on a TESCAN SEM MIRA 3 for the martensitic sample.

The grain boundary misorientation information provided by EBSD can be used to identify the PAGBs. They were identified using the misorientation criterion provided by Morito et al. [50]. In this work, grain boundaries that have misorientation angles between 21.5° to 46.5° are considered as PAGBs as other types of grain boundaries (packet, block, and lath boundaries) are excluded from this range of misorientation due to the orientation relationship of the austenite-martensite phase transformation [50], [56].

TEM thin foils were prepared using FIB (FEI Helios DualBeam 600) as it provides the possibility to prepare lamella at a precise PAGB identified by the misorientation criterion mentioned above. A typical thin foil preparation procedure was done, the final milling current ranges from 920 to 30 pA. The final thickness of each thin foil is around 100 nm to ensure enough signals for STEM-EDX analyses. To ensure no strong oxidation or diffusion that can influence the analyses, each thin foil was analyzed no later than two days after preparation and all samples were always preserved under vacuum with silica gel to reduce humidity. In total, seven FIB thin foils were prepared, among which three on BSC and four on MSC. In principle, each FIB thin foil contains one PAGB and many other grain boundaries. However, one MSC thin foil showed no grain boundaries between 21.5°-46.5° thus a fourth thin foil was prepared. Three PAGBs were analyzed for BSC and MSC.

The TEM used in this study was a FEI Tecnai OSIRIS operating at 200 kV, the beam conditions were adjusted so that the beam diameter was around 1 nm and the beam current was about 0.5 nA. PACOM acquisition was performed using the NanoMEGAS ASTAR system. Acquisition was done on each thin foil so that the PAGB can be re-identified using the same misorientation criteria (21.5°-46.5°) [50] and the misorientation angle of other grain boundaries present in the thin foil can be identified. Figure 2 shows an example of index quality map obtained using PACOM. The grain boundary portions indicated in red have a misorientation in the range of 21.5°-46.5°, meaning that they belong to a PAGB. By continuity, the portions indicated by the blue arrows are also considered as PAGB.

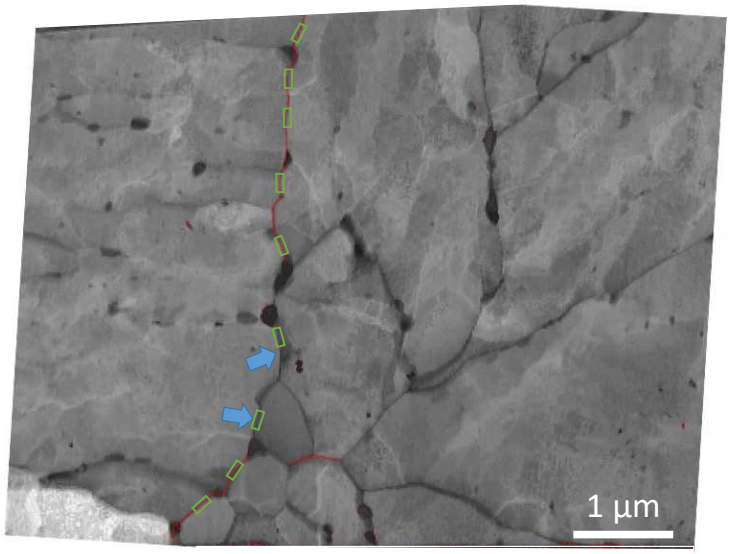

Figure 2: Index quality map of PACOM acquisition for a martensitic thin foil, PAGBs with misorientation angle between 21.5◦ - 46.5◦ are marked in red. The blue arrows show the portions of the PAGB having misorientation outside the range of 21.5° - 46.5°. Green boxes (out of scale) represent the positions of the STEM-EDX acquisitions conducted on different segments of the PAGB.

The analytical system is based on the EDX FEI SuperX using four windowless detectors. The grain boundary was aligned parallel to the incident beam before acquisition. Elemental mapping was acquired using the hypermap function of Esprit v1.9 by Brukers. The mapping size was approximately 161 x 40 or 114 x 40 nm, giving a pixel size of 0.16 or 0.11 nm^2. The acquisition time was usually around 40 minutes for the entire map. The drift correction option in Esprit was used and the drift correction during the acquisitions was around 30 nm on average. These conditions were the same in the authors' previous works [38], [39]. STEM-EDX acquisitions were first performed on each portion of the PAGB, see green boxes in Figure 2. It was considered relevant to perform acquisitions on each PAGB segments because these different segments have different misorientation angle and rotation axes; in other words, they are different in nature. Then, acquisitions were performed on other non-PAGBs present in the thin foil. The selection of these non-PAGBs was somewhat random depending on their alignment with respect to the

incident beam. Table 2 shows the number of TEM thin foils per sample, and the number of EDX acquisitions performed on different types of grain boundaries.

Table 2: Summary of STEM-EDX analysis on different samples and different types of grain boundaries.

Sample	#FIB thin toils	Lath boundary	other LAGB	Portions of PAGB	other HAGB	Σ3
BSC	3	24	7	22	17	0
MSC	4*	9	1	24	10	11
Total	7	33	8	46	27	11

*One of the thin foils for MSC does not contain PAGB, thus a fourth thin foil was prepared.

Figure 3(a) shows the typical EDX acquisition map on a grain boundary with segregations. The STEM-BF image shows that the grain boundary was well-aligned parallel to the incident beam and a portion of each adjacent grain was included in the mapping. The five element maps clearly show that phosphorus, molybdenum, manganese, and nickel segregate at grain boundaries in the studied low alloy steel.

To extract the segregation peaks (P Kα, Mo Lα, Mn Kα, Ni Kα) without the spectrum background and artefacts, the box method proposed previously by the authors [38] was used. This method relies on three box spectra extracted from the STEM-EDX map: one “GB” spectrum containing the segregation signals at the grain boundary (red box in Figure 3(a)) and two “Grain” spectra from each adjacent grain (yellow boxes in Figure 3(a)). The average of the two “Grain” spectra allows obtaining a reference spectrum used for spectrum background removal. Figure 3(b) then shows the superposed EDX spectra of the “GB” spectrum and the reference spectrum obtained from the “Grain” spectra. The segregation of the four elements (marked in red) can be clearly seen while the presence of spurious peaks (notably Zr, Si, Cu [59]) and artefacts (Ga and Pt from FIB preparation) were removed by the reference spectrum. The net P Kα, Mo Lα, Mn Kα, and Ni

Kα peaks were obtained by subtracting the reference spectrum from the GB one (see Figure 3(c)). Gaussian functions were fitted to the peaks to determine the four peak intensities. The iron peak intensity was obtained in the same manner by fitting a Gaussian function to the iron Kα peak directly on the "GB" spectrum.

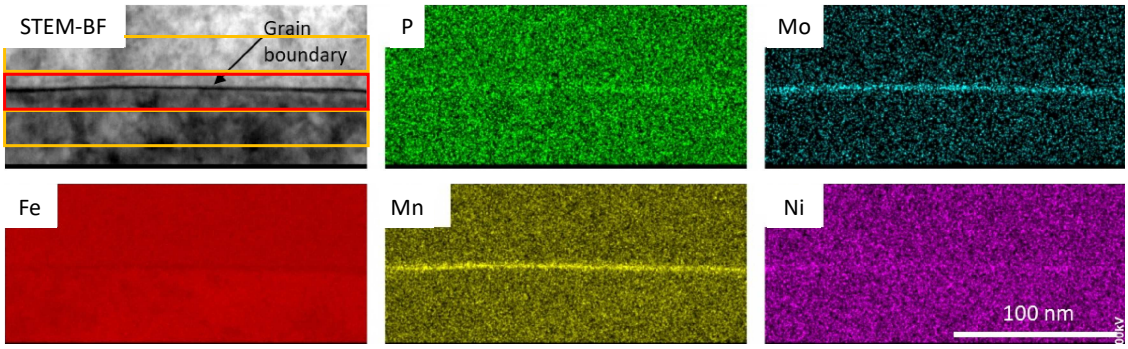

(a)

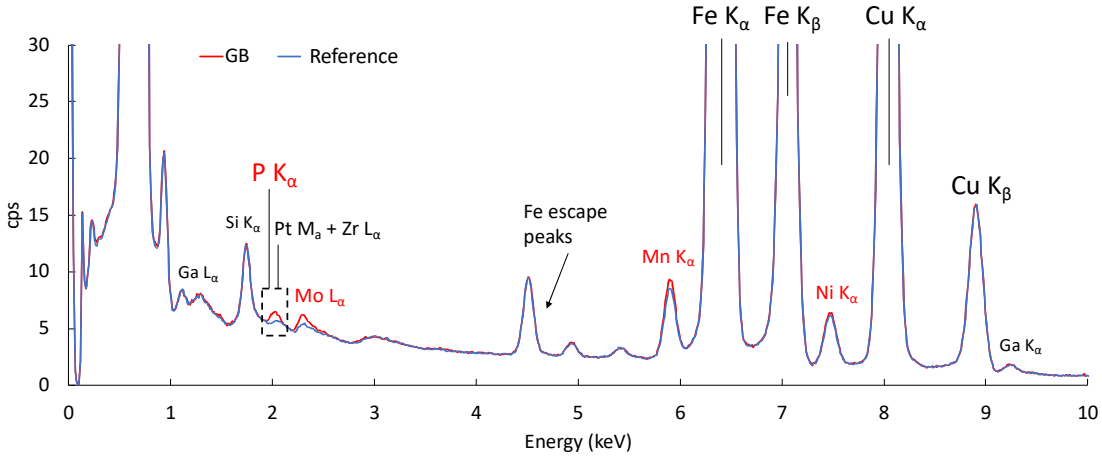

(b)

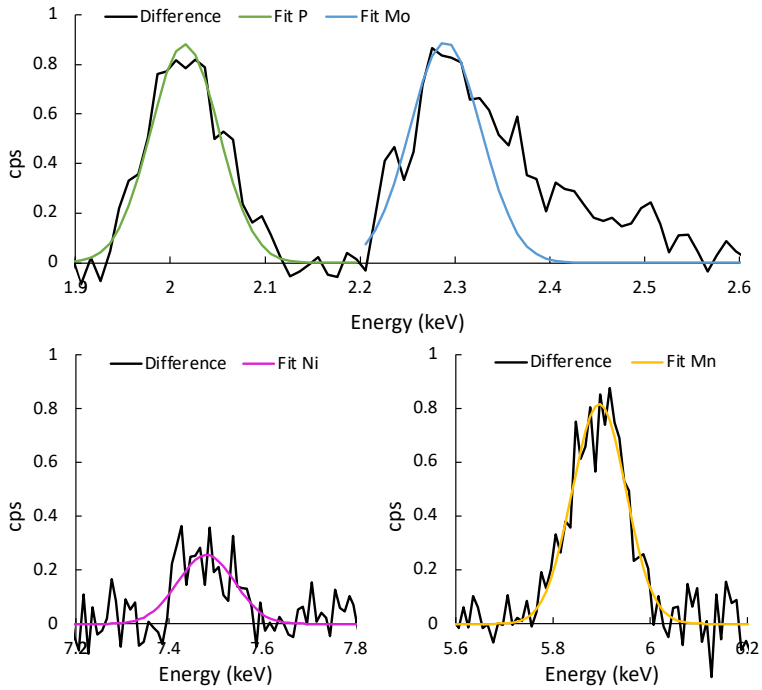

(c)

Figure 3: Example of STEM-EDX grain boundary analysis on 16MND5 steel. (a) STEM-BF image showing the grain boundary and the element qualitative mappings, (b) superposed GB spectrum and reference spectrum showing segregations of P, Mo, Mn, and Ni, (c) net P Kα, Mo Lα, Mn Kα, and Ni Kα peaks after background subtraction (GB spectrum minus reference spectrum) fitted by a Gaussian function.

The Cliff-Lorimer [60] method is used to quantify the segregated elements, the adapted formula is [38]:

$$C_i = \frac{k_{i/Fe} * ACF_{i/Fe} * \frac{I_i}{I_{Fe}}}{1 + \sum_i \left(k_{i/Fe} * ACF_{i/Fe} * \frac{I_i}{I_{Fe}} \right)} \quad (1)$$

where C_i is the concentration of element i (P, Mo, Mn, Ni), $k_{i/Fe}$ is the k factor of element *i* with respect to iron, $ACF_{i/Fe}$ is the absorption correction factor of element *i* with respect to iron, $\frac{I_i}{I_{Fe}}$ is the intensity ratio of the element *i* Kα or Lα peak and Fe Kα peak. The k factors used in this study are: $k_{P/Fe} = 0.790$ [38], $k_{Mo(L\alpha)/Fe} = 2.601$, $k_{Mn/Fe} = 0.919$ [61], and $k_{\mathrm{Ni}/Fe} = 1.125$.

$k_{Mo(L\alpha)/Fe}$ and $k_{\mathrm{Ni}/Fe}$ are values given by the JEOL software (a TEM also operating at 200 kV). The reason of choosing these values is because the JEOL software proposes values that are closer to the measured $k_{P/Fe}$ and to the values given in [61] compared to other sources. ACF for each element are calculated based on the same method mentioned in [38], [62]. The interface segregation can be expressed in atom/nm^2 using [32], [38]:

$$S_i = wN\frac{A_{Fe}}{A_i}C_i \qquad (2)$$

where S_i is the interface concentration of element *i* in atom/nm^2, N is the matrix density in nm^{-3} (85.5 nm^{-3} for iron), A_{Fe} and A_i are the atomic mass of iron and element *i*, respectively, *w* is the GB box width. The unit atom/nm^2 was chosen so that the provided intergranular segregation quantification can be free from hypothesis such as grain boundary thickness needed for at% or wt% or Miller's index of the segregation plane needed for the monolayer coverage. The "GB" box width was optimized case by case to ensure the minimum width that contains all signals from the grain boundary was selected. The counting error and detection limit of the method are of the order of 0.1 atom/nm^2. More details can be found in the authors' previous work [38].

3. Microstructure Investigation

Figure 4(a) shows the optical micrograph of the as-quenched martensitic sample where the needle-shaped laths can be clearly seen. This observation ensures the water quench cooling rate being fast enough to obtain martensitic microstructure of the studied material. Figure 4(b) then shows the optical micrograph of the step cooled martensitic sample (MSC) where carbide precipitates are visible. Figure 2(c) shows the optical micrograph of the step cooled bainitic

sample (BSC) where carbide clusters located within the ferritic grains can be seen. Although the microstructure of the base metal of similar grade steel is commonly believed to be upper bainite [63]–[65], Figure 2(c) resembles the granular bainite proposed by Zajac *et al.* [54]. A possible explanation of the formation of these carbide clusters is the presence of "retained austenite and martensite islands (M-A constituents)" after quenching that have higher carbon content. It is known that the tempering treatment dissolves M-A constituents and forms carbides [51].

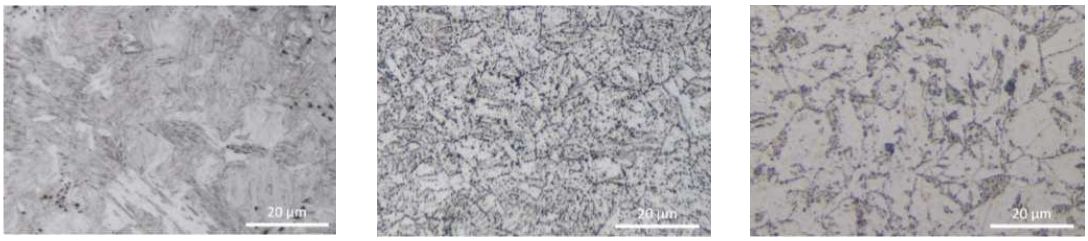

(a) *(b)* *(c)*

Figure 4: Optical micrograph of chemically etched sample surfaces showing grain boundaries and carbides of (a) as-quenched martensite, (b) step cooled tempered martensite (sample MSC), (c) step cooled tempered bainite (sample BSC).

Figure 5(a) and (b) show the EBSD orientation map of the two step cooled samples. The misorientation angle threshold for grain construction was chosen to be 3°. Figure 5(c) and (d) show the grain boundary map, where ferritic grain boundaries (i.e., block and packet boundaries), PAGBs and Σ3 boundaries are marked in different colors. The PAGBs marked out in Figure 5(c) and (d) are based solely on the misorientation criteria (21.5° - 46.5°) [50]. Then, Figure 5(e) and (f) shows the reconstruction of prior austenite grains using the iterative method proposed by Nyyssönen *et al.* [66], implemented in the MTEX environment [67]. It can be seen in Figure 5(c) and (d) that there are more Σ3 boundaries in martensite than in bainite, which was expected. It is also observed that the reconstructed prior austenite grains (Figure 5(e) and (f)) basically follows the red PAGBs marked in Figure 5(c) and (d).This further indicates that the misorientation criteria used to identify PAGB in this work can be applied to both microstructures.

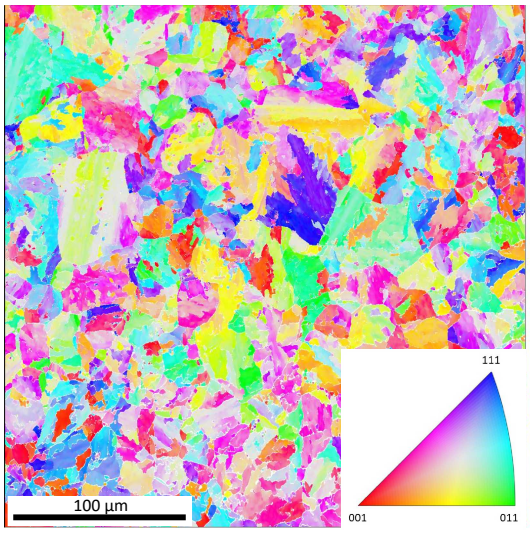
111
001
011
100 µm

(a)

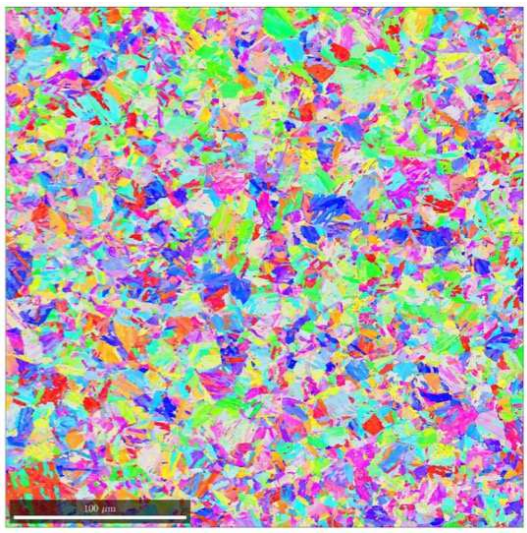

(b)

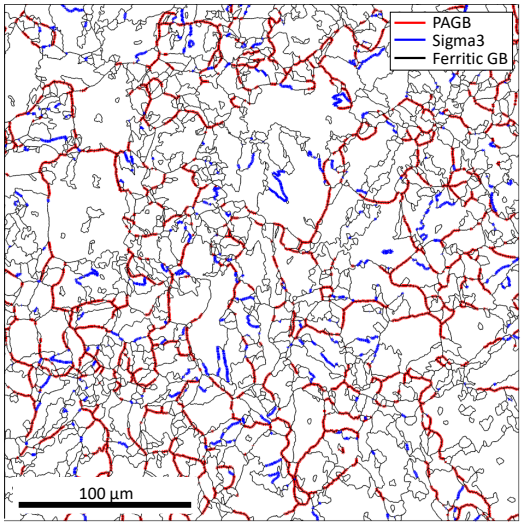
PAGB
Sigma3
Ferritic GB
100 µm

(c)

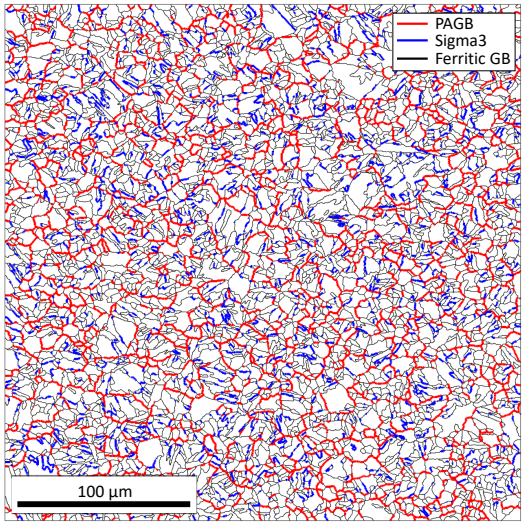
PAGB
Sigma3
Ferritic GB
100 µm

(d)

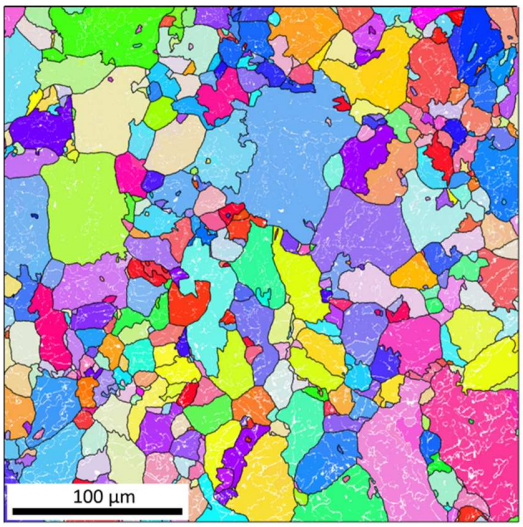
100 µm

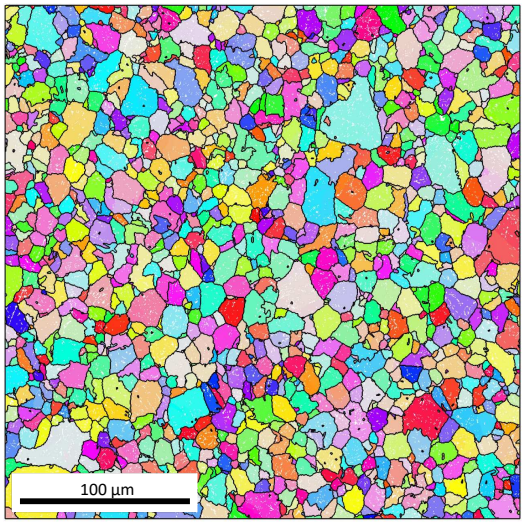
100 µm

(e) (f)

Figure 5: Mappings obtained from EBSD acquisitions: orientation map for (a) BSC and (b) MSC; Ferritic grain boundaries (i.e., block and packet boundaries), PAGBs and Σ3 boundaries for (c) BSC and (d) MSC; prior austenite grain reconstruction for (e) BSC and (f) MSC.

The prior austenite grain size was determined from the EBSD orientation maps using the interception method; the ferritic (block) grain size was determined automatically from the EBSD acquisitions (see Table 3). For the martensitic microstructure, the obtained prior austenite grain size is similar to the one obtained by Pous-Romero and Bhadeshia. [68] after similar austenitization temperature and duration. The bainitic sample, on the other hand, presents an austenitic grain size that is twice that of the martensitic sample. In the study of Pous-Romero [68], it can be seen that the composition, austenitization temperature, and duration can all influence the austenite grain size. As the bainitic samples were directly cut from an industrial shell with greater thickness, the level of uncertainty on the austenitization temperature and time are higher than for the martensitic sample. This may explain why the PAG size was found larger in the bainitic sample. The determination of lath sizes was done using the interception method on STEM-BF images as laths are barely visible in the EBSD maps. A typical STEM-BF image of the samples is presented in Figure 6 (a) and (b).

Table 3: Different grain sizes in bainitic and martensitic 16MND5 steel studied in this work.

Sample	Prior austenite grain (µm)	Ferrite grain (µm)	Lath (µm)
BSC	19.3	4.2	0.6
MSC	9.1	3.1	0.4

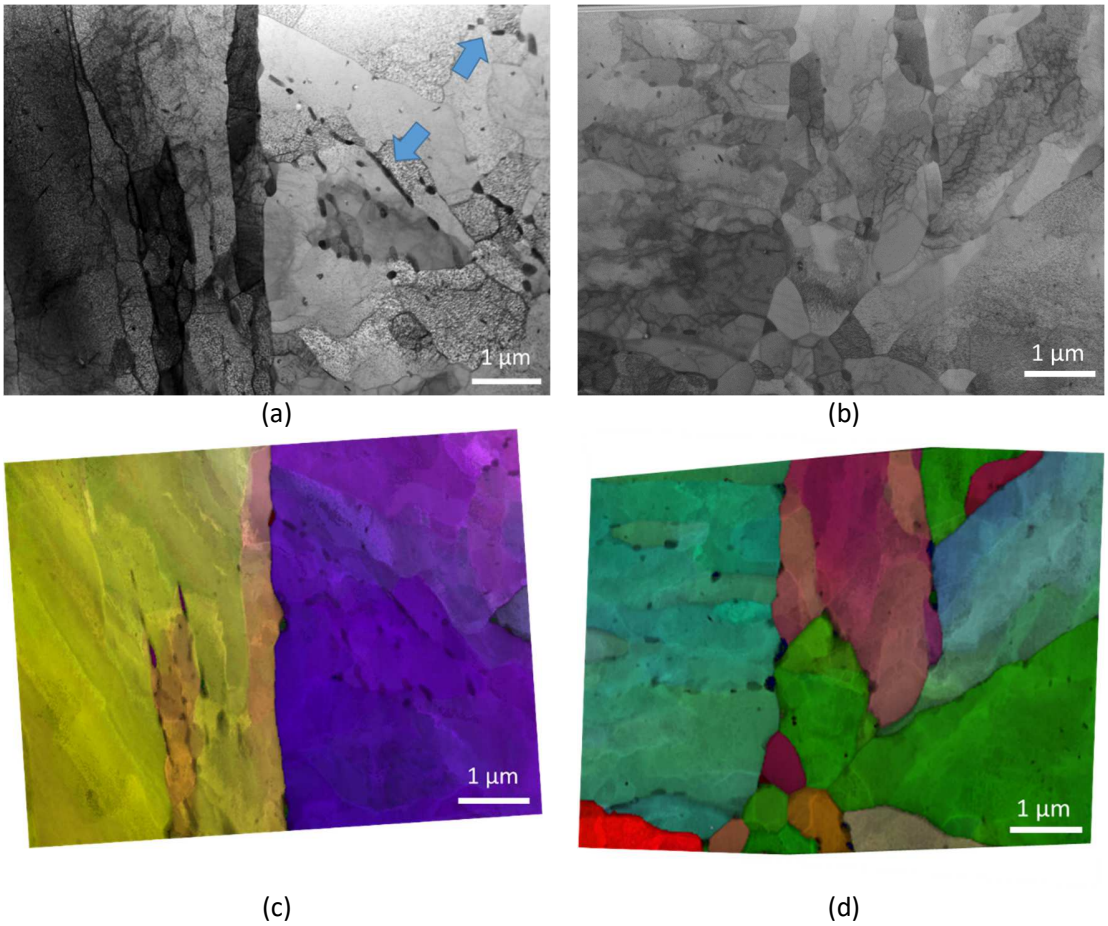

(a) (b)

(c) (d)

Figure 6: STEM Bright Field (BF) image of a TEM thin foil of a (a) BSC thin foil and a (b) MSC thin foil. (c) and (d) are corresponding PACOM orientation map overlapped with index quality map. The blue arrows in (a) points out carbide clusters present in the bainitic microstructure.

Figure 7(a) and (b) show the grain boundary misorientation angle distribution of the two samples respectively. For BSC, there are two high peaks near 60° and 54° (green box and yellow arrows in Figure 7(a) respectively); For MSC, only one high peak around 60° (green box in Figure 7(b)) is present. This high peak in martensite suggests more abundant twin boundaries of 60° $\langle 111 \rangle_{\alpha}$, i.e., Σ3 boundaries, while the height of the peak at 54° (yellow arrow in Figure 7(b)) is significantly lower. The distributions of grain boundary misorientation angle in this work are similar to those obtained by Gourgues *et al.* [56]. Those authors suggested that the misorientation distribution between *upper* bainite and martensite can be distinguished by the

height ratio between the peaks at 54° and 60°; on the other hand, *lower* bainite should have a similar distribution to martensite. From Figure 7(a) and (b), it is very obvious that the height ratio between the peaks at 54° and 60° for bainite microstructure is higher than that for martensite microstructure, which again confirms that the studied microstructures are upper bainite and martensite. Considering that the bainitic sample (BSC) was extracted from the original microstructure, this observation also agrees with the common microstructure observation of similar grade steels in the literature [63]–[65].

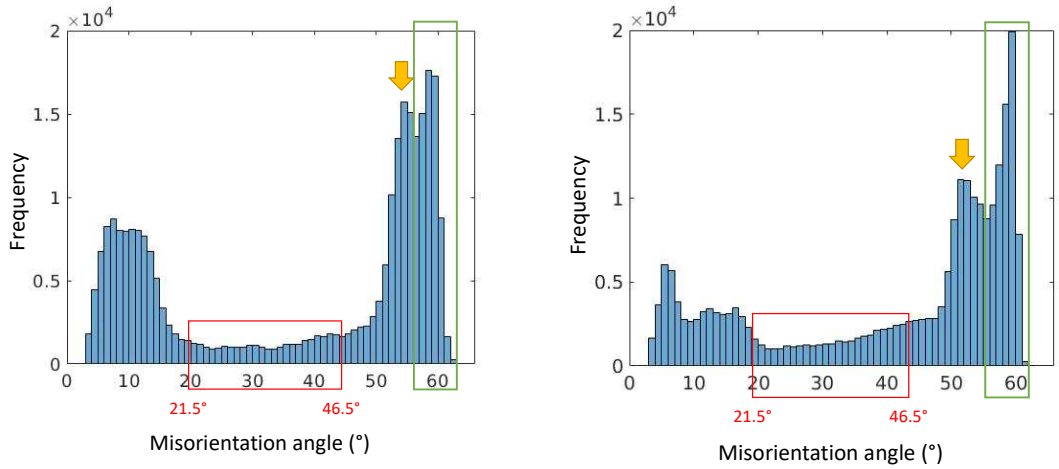

Figure 7: Grain boundary misorientation distribution histogram of (a) bainite (sample BSC), (b) martensite (sample MSC).

Figure 8 shows the distribution of grain boundary rotation axes for bainite and martensite in three different misorientation ranges. The 21.5°-46.5° range (red rectangles in Figure 7) contains in principle only PAGBs. Figure 8 shows a random distribution of the rotation axes in that range, which is consistent with the PAGB nature of those grain boundaries. It can also be noted that the misorientation angle distribution is relatively flat in this range (see red boxes in Figure 7(a) and (b)). More distinctive differences can be observed for misorientation angles in the ranges of 46.5°-56° and 56°-63°, corresponding to the two high misorientation peaks of Figure 7. The

bainitic microstructure does not present a high density of [111] or [110] rotation axes at any misorientation (see Figure 8(a)). The high density zones seem to be in the middle of [111] and [110], which have a rotation axis close to [221] and [331] for misorientation between 46.5°-56°; while rotation axes are more shifted toward [011] close to [331] and showing a secondary hot zone close to [443] for misorientation above 56°. The martensitic microstructure, on the other hand, shows three hot zones for the range of 46.5°-56°, around [111], [011] and [331]. This already shows a distinctive difference with the bainitic structure; there is also a high density of [111] and [110] rotation axes for misorientation above 56° (see Figure 8(b)), which are not seen for the bainitic structure. This indicates the high population of Σ3 boundaries compared to bainite, as suggested in [8], [56].

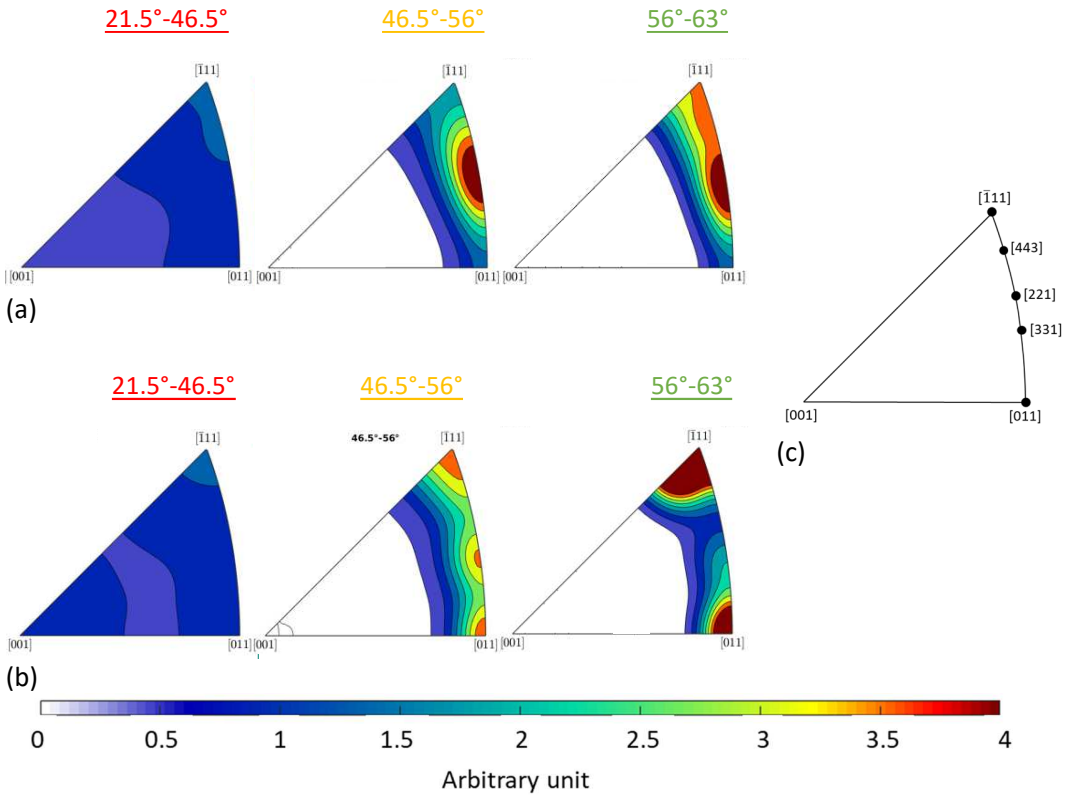

Figure 8: Rotation axis distribution in the different misorientation angle ranges for (a) bainite (sample BSC), (b) martensite (sample MSC). (c) Theoretical location of main rotation axes between [110] and [111].

STEM-BF images of one of the BSC thin foils and one of the MSC thin foils are shown in Figure 6(a) and (b), respectively. Figure 6(c) and (d) shows the corresponding orientation maps (overlapped with the index quality map) obtained using the PACOM acquisitions. The reason to show an overlapped map instead of only showing the orientation map for PACOM acquisitions is due to the low misorientation between the laths. The orientation map often presents little color differences making the identification of the lath boundaries complicated, for example in Figure 6(c).

For both thin foils presented in Figure 6, it can be seen that the form of the laths can be different depending on the direction. They seemed elongated in the left grain Figure 6(c), but rather isotropic in Figure 6(d). This is related to the lath orientation with respect to the thin foil.

Carbide clusters of different sizes were observed in the studied low alloy steel. Larger ones as shown in Figure 2(c) can be observed using optical microscopy and smaller ones were observed on TEM thin foils, see blue arrows in Figure 6(a). It can be seen that large carbides (hundreds of nms) form a cluster that is located only on the middle right, and another one that is on the top right corner of the thin foil. Some other smaller precipitates can also be seen in Figure 6(a). STEM-EDX was used to identify the chemical composition of the different carbides. The results show typical carbides in this low alloy steel that were also observed in [69]. These include cementite (Fe_3C) that is rich in Mn; another one rich in Mo is believed to be Mo_2C. The same carbides were observed in the martensitic thin foils. More detailed investigations for the carbides were not performed in this study since the focus was mainly on intergranular segregation measurements.

4. STEM-EDX Analysis of Grain Boundary Segregation

In this work, 132 different grain boundaries were analyzed using STEM-EDX. For each grain boundary, the misorientation angle was obtained using PACOM. The quantification of phosphorus, molybdenum, manganese, and nickel segregation at the 132 grain boundaries analyzed in the two studied microstructures (bainite and martensite tempered and aged by step cooling) are presented in Figure 9. The error bar shown is the standard deviation of each group of grain boundaries. The analyzed grain boundaries are categorized into five different groups depending on the misorientation angle:

1. Lath boundaries: misorientation below 7°,

2. Other LAGBs: misorientation between 7 - 15°,

3. PAGBs: misorientation between 21.5° - 46.5° [50]. The PAGBs defined by continuity (see blue arrows in Figure 2), which are not in the 21.5° - 46.5° range, were also included in this category,

4. Other HAGBs: grain boundaries with misorientation angle above 15° but not PAGBs,

5. Σ3 boundaries.

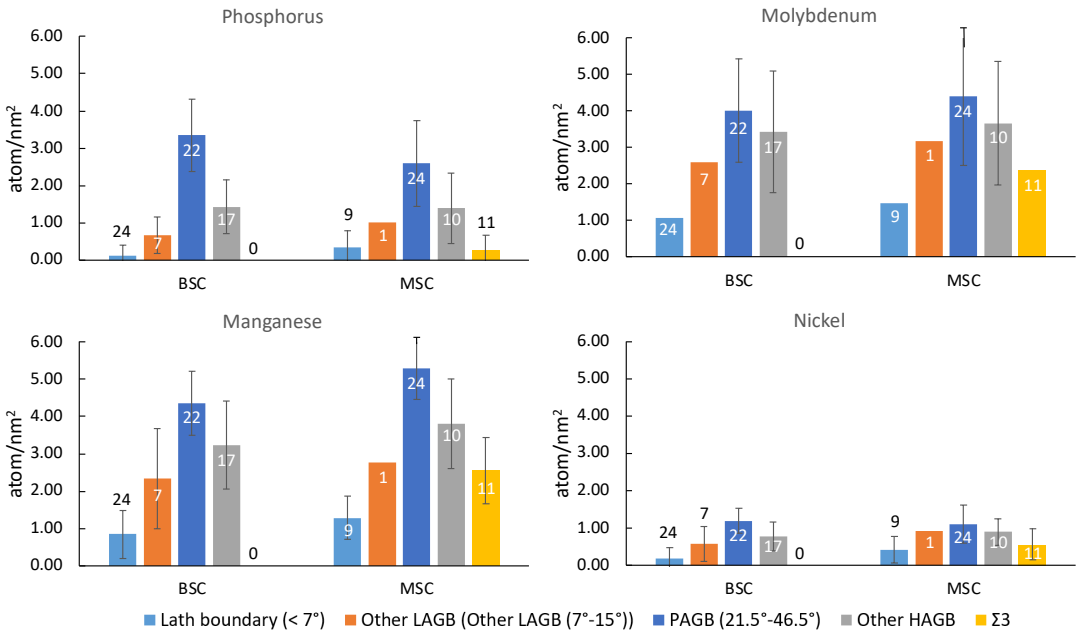

Figure 9: Concentration of each element at different types of grain boundaries for the two samples (BSC & MSC). The error bars are the standard deviation in each group. The numbers indicated on the bars represent the number of grain boundaries analyzed in each group (also shown in Table 2). The groups containing 0 or 1 measurement do not have an error bar. For MSC, the standard deviation of certain series of measurements was forced very large and could hence not be shown in the figure.

Figure 9 shows that P, Mo, Mn, and Ni segregate at all types of grain boundaries in both bainite and martensite. In any case, it can be seen that PAGBs have the highest segregation level and that lath boundaries have the lowest. It is remarkable that the segregation levels in the different grain boundary categories always follow the same ranking: PAGB > Other HAGBs > Other LAGBs > Lath boundaries. This is true for all the elements in the two microstructures (bainite and martensite). This result is a quantitative and statistically sound confirmation of the common assumption that in bainitic and martensitic steels, PAGBs are more prone to segregation than any other types of boundaries [8], [11], [24], [25]. This has to be related to the more random nature of PABGs, the other grain boundary types being constrained by particular orientation

relationships obeyed by the martensitic or bainitic transformation, like Kurdjumov-Sachs (KS) or Nishiyama-Wassermann (NW) for example.

In principle, block and packet boundaries have only a limited number of possible misorientation angles and rotation axes, as listed by Gourgues *et al.* [56] for the KS and NW relationships. An attempt was made in this work to identify individually block and packet boundaries by comparing their misorientation angle and rotation axis obtained using PACOM with the theoretical ones listed by Gourgues *et al.* [56]. However, no strict correspondence could be obtained, possibly because of experimental uncertainties and/or deviation of the orientation relationship from strictly KS or NW. Hence, block and packet boundaries could not be individually identified in this work. Apart from the Σ3-type boundaries, all the other block and packet boundaries are gathered in the "Other LAGBs" and "Other HAGBs" categories. It is clear from Figure 9 that block and packet boundaries have segregation levels intermediate between PAGBs and lath boundaries.

Apart from PAGBs and Σ3 boundaries, a clear correlation between the level of segregation and the misorientation angle is observed: Other HAGBs (> 15°) > Other LAGBs (7°-15°) > Lath boundaries (< 7°). Again, this is true for all the four elements segregated at the grain boundaries. This correlation between segregation and misorentation is in agreement with the results from Zhang *et al.* [30] obtained using atom probe tomography measurements on different grain boundaries in a 16MND5 weld. It should be mentioned however that the segregation levels measured in a given grain boundary category are quite widely scattered (see the standard deviation bars in Figure 9). In other words, for two grain boundaries with very close misorientation, significantly different levels of segregation can be found.

As Σ3 boundaries are very rare in bainite, no Σ3 boundary was analyzed in BSC. In contrast, 11 Σ3 boundaries were analyzed in sample MSC. It can be seen that all four elements segregate at Σ3 boundaries, and segregation levels for Mo, Mn, and Ni are only slightly lower than for the group "Other LAGBs". On the contrary, the P segregation level at Σ3 boundaries is low (lower than lath boundaries). However, significant scatter was found among the 11 measurements: seven of them have no detectable phosphorus segregation, whereas among the four other measurements, the phosphorus segregation can go up to 0.99 atom/nm^2, which is nearly half of the average segregation at PAGBs and is very significant. In summary, these measurements show that Σ3 boundaries are not necessarily free from phosphorus segregation, which is in contrast to what the literature suggested [8].

Considering the four segregated elements, phosphorus is not the most segregated element regardless of it being identified as the cause of RTE. The highest phosphorus segregation measured was around 3 atom/nm^2 at PAGBs in both microstructures. Manganese and molybdenum levels are the highest among the four at any analyzed grain boundary, probably due to their high bulk concentration (see Table 1). Very high standard deviation is observed for molybdenum measurements compared to other elements. The maximum molybdenum concentration can be up to four times higher than the minimum value. These extreme cases were not common, but no further investigations were done as it was not the focus of this work.

From the analyzed grain boundaries in the two studied microstructures, the intergranular segregation induced by step cooling simulating thermal aging remained very similar in bainite and martensite. The segregation level of each element between the two microstructures is very close disregarding the grain boundary group. This overwrites the hypothesis given in the literature that the phosphorus segregation behavior would be different in bainite and

martensite [8], [11]. In contrast, the results of this work show that the phosphorus intergranular segregation level does not vary between microstructures and thus does not play a primary role in the different microstructure susceptibility to RTE.

It was also suggested that trapping of phosphorus is higher in bainite than in martensite [8], [11], which could explain the better resistance to RTE of bainite by less segregation at PAGBs. To further verify this assumption, the amount of phosphorus trapped in the different types of grain boundaries was determined for the two microstructures. To have a simple approach, only three types of grain were considered: PAG, laths and ferrite grains (including blocks and packets). Laths were assumed to have an elongated "fries" shape, whereas PAG and ferrite grains are considered isotropic.

The grain boundary density (grain boundary area per unit volume) is 3/d for isotropic grains and 2/d for "fries" grains, where d is the grain size. The concentration of trapped phosphorus (in atom/nm^2) can be easily obtained by multiplying the grain boundary density by the phosphorus grain boundary concentration. This trapped phosphorus concentration can then be converted into wt ppm and compared to the nominal phosphorus content (80 wt ppm). Table 4 shows the calculation of the trapped phosphorus at different types of grain boundaries for the two samples. The grain size of the different types of grains are from Table 3. Figure 10 shows the pie charts of how the phosphorus is distributed between the bulk and the different types of grain boundaries for both samples. It can be seen that the total phosphorus trapped by different grain boundaries is rather low and not very different in the two microstructures (~15% in bainite and ~25% in martensite). This further supports that the microstructure susceptibility to phosphorus intergranular segregation is similar between bainite and martensite. It is to be noted that the two microstructures do not have the same PAG size, but the effect of grain size

to the trapping calculation is very little. The main difference shown in Table 4 comes from trapping by lath boundaries, where martensite has smaller lath size and a significant higher measured segregation level. However, segregation measurements for lath boundaries present large standard deviation, so the trapping at lath boundaries may be overestimated.

Table 4: Phosphorus trapped in different types of grain boundaries in bainite & martensite. Grain sizes are from Table 3.

Sample	Grain boundary type	Grain size (d) (μm)	GB density (m^2/m^3)		P intergranular segregation concentration ($atoms/nm^2$)	Trapped phosphorus			
						atoms /nm^3	at ppm	wt ppm	%*
BSC	PAGB	19.3	3/d	1.5×10^5	3.35	5×10^{-4}	6.1	3.4	4.2%
	Other GB	4.2	3/d	7.2×10^5	1.2	9×10^{-4}	10.0	5.6	7.0%
	Lath boundaries	0.6	2/d	3.2×10^6	0.12	4×10^{-4}	4.5	2.5	3.1%
Total						**1.8×10^{-3}**	**20.6**	**11.5**	**14.3%**
MSC	PAGB	9.1	3/d	3.2×10^5	2.60	9×10^{-4}	10.0	5.6	7.0%
	Other GB	3.1	3/d	9.6×10^5	0.82	8×10^{-4}	9.2	5.1	6.4%
	Lath boundaries	0.4	2/d	4.5×10^6	0.35	1.6×10^{-3}	18.4	10.2	12.8%
Total						**3.2×10^{-3}**	**37.7**	**20.9**	**26.2%**

*Percentage calculated based on the nominal content (80 wt ppm)

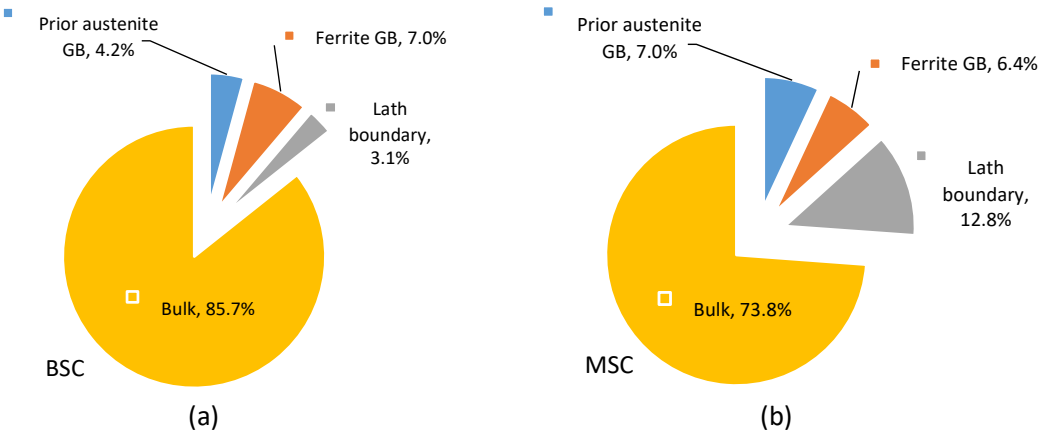

Figure 10: Trapping of phosphorus at different types of grain boundaries for (a) sample BSC, (b)

sample MSC.

To understand the correlation between different solutes, the measured concentrations of each element (P, Mn, Mo, and Ni) at each grain boundary were plotted against each other. Figure 11(a) shows the correlation between two elements (six possible combinations) in bainite and in martensite. Each dot represents one analyzed grain boundary. The color code of different grain boundary group remains the same as Figure 9. It is clearly shown that P concentration increases as Mn or Ni concentration increases in both bainite and martensite (Figure 11(a)). In other words, when comparing two different grain boundaries with different phosphorus contents, the grain boundary containing more phosphorus also contains more nickel and more manganese. When comparing the three solutes with Mo (Figure 11(b)), the dots are more dispersed. Mo does not seem to have any relationship with either of the elements in both microstructures (although a slight correlation with Mn might be suspected).

Among the different analyzed grain boundaries, the grain boundary characteristics change, meaning that the number of available site changes from one grain boundary to another. The correlations observed in Figure 11(a) suggests that P, Mn, and Ni indeed segregate to the same grain boundary sites: when a given grain boundary offers a high number of segregation sites, a correlated increase of P, Mn, and Ni concentration is observed. On the other hand, Figure 11(b) shows the quasi-absence of correlation between Mo and the other elements, suggesting that this element segregates to different sites. This is in agreement with ab-initio simulations by Paré *et al.* [70] showing that Mo segregates preferentially to sites in tension in the grain boundary, in contrast to P segregating to sites in compression.

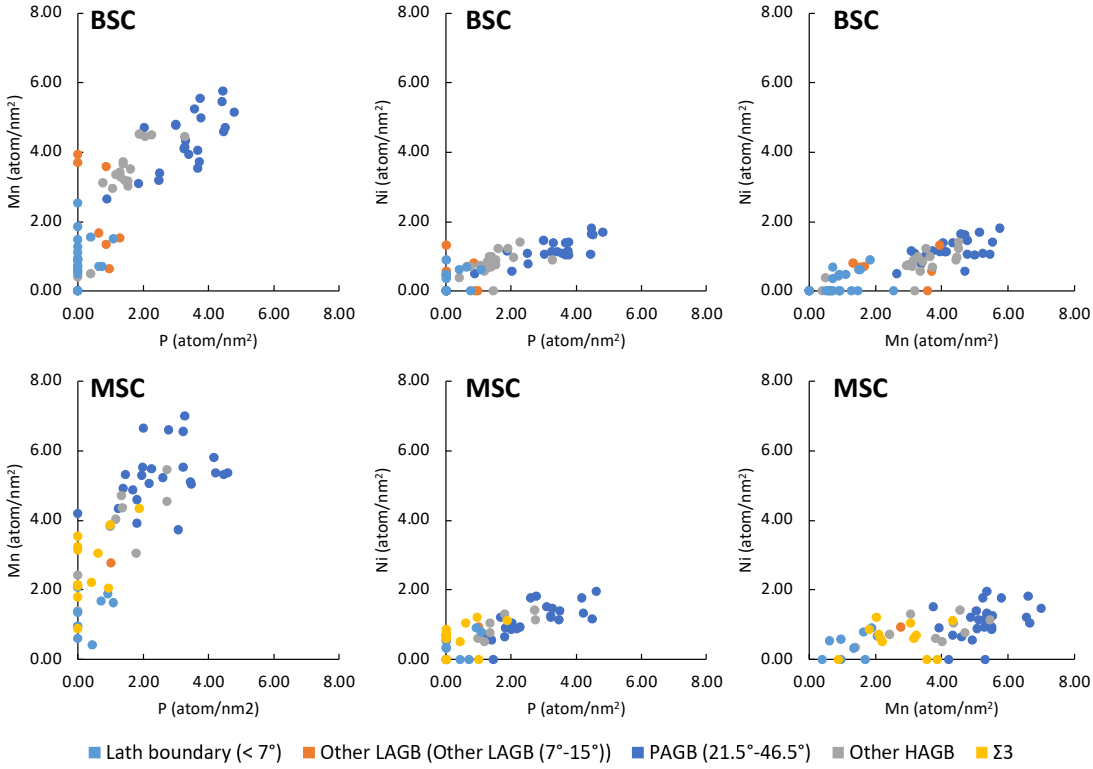

(a)

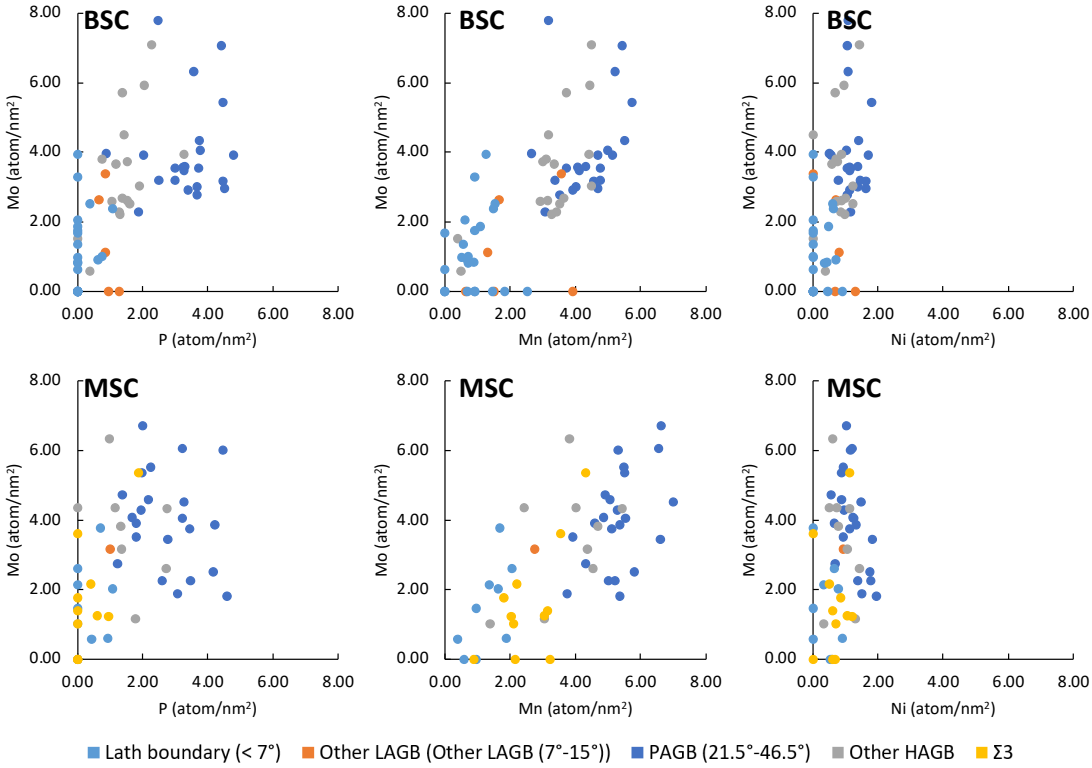

(b)

Figure 11: Correlation between segregation of each element in atom/nm² measured at each

analyzed grain boundary in the two studied samples. The different color code represents the different category of grain boundaries (same as in Figure 9). (a) relations between P, Mn, Ni, (b) relations between Mo and the other three elements. The maximum values on both axes are adjusted to be the same in both figures to facilitate comparison. Note that only two dots in (b) are excluded due to this adjustment.

5. Conclusions

This study investigates the microstructure susceptibility to intergranular segregation of a quenched and tempered 16MND5 (SA508 Cl.3) steel with a bainitic or a martensitic microstructure. Chemical etching and EBSD investigations confirm that the studied microstructures are upper bainite and martensite. They present different carbide distributions and distinctive grain boundary misorientation distribution. The results showed that martensite has a higher population of high coincidence boundaries than bainite. In order to obtain statistically reliable results, a large number (132) of different types of grain boundaries were quantitatively analyzed using a STEM-EDX method developed in previous works. It was shown that phosphorus, manganese, molybdenum, and nickel segregate to all types of grain boundaries in both microstructures. Results have shown that PAGBs are the most susceptible and lath boundaries are the least susceptible to segregation. Other grain boundaries show intermediate levels of segregation. Also, it has been shown that high coincidence boundaries (i.e., Σ3) present segregation with a concentration not necessarily much lower compared to other grain boundaries. Also, the phosphorus intergranular segregation level remained quite low (≈3 atom/nm^2) even after step cooling. The trapping effect, i.e., the bulk depletion of phosphorus due to grain boundary segregation, was estimated in both tempered martensitic and tempered bainitic microstructures. It was shown that the total phosphorus content segregated at the different types of grain boundaries does not exceed 25% of the nominal content (80 wt ppm). It was concluded that this effect is not expected to strongly affect the

phosphorus segregation behavior. Among the four segregated elements, it was observed that P, Mn, and Ni most likely occupy the same type of segregation site, while Mo occupies different sites. The different analyses showed that the studied bainitic and martensitic microstructures of the same low alloy steel have very similar behavior of solute intergranular segregation. The different RTE susceptibility of bainitic and martensitic pressure vessel steel led some authors to assume that those two microstructures had different solute grain boundary segregation behaviors. The quantitative study presented in this paper contradicts this assumption and suggests that the grain boundary segregation alone cannot explain the different susceptibility degrees of bainite and martensite to RTE.

6. Funding

This research was mainly funded by EDF (Electricité de France) with the support of ANRT (Association Nationale de la Recherche et de la Technologie)

7. References

[1] M. A. Islam, “Grain Boundary Segregation Behavior in 2.25Cr-1Mo Steel During Reversible Temper Embrittlement,” *J of Materi Eng and Perform*, vol. 16, no. 1, pp. 73–79, Feb. 2007, doi: 10.1007/s11665-006-9011-1.

[2] H. Nakata, K. Fujii, K. Fukuya, R. Kasada, and A. Kimura, “Grain Boundary Phosphorus Segregation in Thermally Aged Low Alloy Steels,” *Journal of Nuclear Science and Technology*, vol. 43, no. 7, pp. 785–793, Jul. 2006, doi: 10.1080/18811248.2006.9711160.

[3] M. Boåsen *et al.*, “Thermal ageing of low alloy steel weldments from a Swedish nuclear power plant – a study of mechanical properties,” presented at the Fontevraud 9, 2018, p. 9.

[4] S. G. Druce, G. Gage, and G. Jordan, “Effect of ageing on properties of pressure vessel steels,” *Acta Metallurgica*, vol. 34, no. 4, pp. 641–652, Apr. 1986, doi: 10.1016/0001-6160(86)90179-3.

[5] C. Naudin, J. M. Frund, and A. Pineau, “Intergranular fracture stress and phosphorus grain boundary segregation of a Mn-Ni-Mo steel,” *Scripta Materialia*, vol. 40, no. 9, pp. 1013–1019, Apr. 1999.
[6] H. Pous-Romero, I. Lonardelli, D. Cogswell, and H. K. D. H. Bhadeshia, “Austenite grain growth in a nuclear pressure vessel steel,” *Materials Science and Engineering: A*, vol. 567, pp. 72–79, Apr. 2013, doi: 10.1016/j.msea.2013.01.005.
[7] T. S. Byun, J. H. Hong, F. M. Haggag, K. Farrell, and E. H. Lee, “Measurement of through-the-thickness variations of mechanical properties in SA508 Gr.3 pressure vessel steels using ball indentation test technique,” *International Journal of Pressure Vessels and Piping*, vol. 74, no. 3, pp. 231–238, Dec. 1997, doi: 10.1016/S0308-0161(97)00114-2.
[8] S.-G. Park, K.-H. Lee, M.-C. Kim, and B.-S. Lee, “Effects of boundary characteristics on resistance to temper embrittlement and segregation behavior of Ni–Cr–Mo low alloy steel,” *Materials Science and Engineering: A*, vol. 561, pp. 277–284, Jan. 2013, doi: 10.1016/j.msea.2012.10.078.
[9] K. D. Haverkamp, K. Forch, K.-H. Piehl, and W. Witte, “Effect of heat treatment and precipitation state on toughness of heavy section Mn-Mo-Ni-steel for nuclear power plants components,” *Nuclear Engineering and Design*, vol. 81, no. 2, pp. 207–217, Sep. 1984, doi: 10.1016/0029-5493(84)90008-6.
[10] D.-D. Shen, S.-H. Song, Z.-X. Yuan, and L.-Q. Weng, “Effect of solute grain boundary segregation and hardness on the ductile-to-brittle transition for a Cr–Mo low-alloy steel,” *Materials Science and Engineering: A*, vol. 394, no. 1–2, pp. 53–59, Mar. 2005, doi: 10.1016/j.msea.2004.10.036.
[11] S. Raoul, B. Marini, and A. Pineau, “Effect of microstructure on the susceptibility of a 533 steel to temper embrittlement,” *Journal of Nuclear Materials*, p. 7, 1998.
[12] P. Lejcek, *Grain boundary segregation in metals*. in Springer Series in Materials Science, no. 136. Berlin: Springer-Verlag, 2010.
[13] B. Gurovich *et al.*, “Influence of structural parameters on the tendency of VVER-1000 reactor pressure vessel steel to temper embrittlement,” *Journal of Nuclear Materials*, vol. 435, no. 1–3, pp. 25–31, Apr. 2013, doi: 10.1016/j.jnucmat.2012.12.020.
[14] M. K. Miller, R. Jayaram, and K. F. Russell, “Characterization of phosphorus segregation in neutron-irradiated Russian pressure vessel steel weld,” *Journal of Nuclear Materials*, vol. 225, pp. 215–224, 1995, doi: https://doi.org/10.1016/0022-3115(94)00667-9.
[15] Y. Nishiyama, K. Onizawa, and M. Suzuki, “Phosphorus Segregation and Intergranular Embrittlement in Thermally Aged and Neutron Irradiated Reactor Pressure Vessel Steels,” presented at the Effects of Radiation on Materials: 23rd International Symposium, ASTM International, 2008. Accessed: Sep. 10, 2022. [Online]. Available: https://www.astm.org/stp46566s.html
[16] R. Pelli and J. Forstén, “Effect of thermal ageing on impact ductility of the nuclear reactor pressure vessel steel SA533B and its weld metal,” *Theoretical and Applied Fracture Mechanics*, vol. 8, no. 1, pp. 25–31, Aug. 1987, doi: 10.1016/0167-8442(87)90015-2.
[17] H. Erhart and H. J. Grabke, “Equilibrium segregation of phosphorus at grain boundaries of Fe–P, Fe–C–P, Fe–Cr–P, and Fe–Cr–C–P alloys,” *Metal Science*, vol. 15, no. 9, pp. 401–408, Sep. 1981, doi: 10.1179/030634581790426877.
[18] S. Takayama, T. Ogura, S.-C. Fu, and C. J. McMahon, “The calculation of transition temperature changes in steels due to temper embrittlement,” *Metall Mater Trans A*, vol. 11, no. 9, pp. 1513–1530, Sep. 1980, doi: 10.1007/BF02654515.
[19] I. A. Vatter, C. A. Hippsley, and S. G. Druce, “Review of thermal ageing data and its application to operating reactor pressure vessels,” *International Journal of Pressure*

Vessels and Piping, vol. 54, no. 1, pp. 31–48, Jan. 1993, doi: 10.1016/0308-0161(93)90126-E.
[20] F. Christien, R. Le Gall, and G. Saindrenan, “Synergetic effect of hardness and phosphorus grain-boundary segregation on the ductile-to-brittle transition temperature of 17-4 PH steel,” *Metallurgical and Materials Transactions A*, vol. 34, no. 11, pp. 2483–2491, Nov. 2003, doi: 10.1007/s11661-003-0008-1.
[21] G. Saindrenan, R. L. Gall, and F. Christien, *Endommagement interfacial des métaux: ségrégation interfaciale et conséquences*. Ellipses, 2002.
[22] R. A. Mulford, C. J. Mcmahon, D. P. Pope, and H. C. Feng, “Temper embrittlement of Ni-Cr Steels by phosphorus,” *Metall Mater Trans A*, vol. 7, no. 8, pp. 1183–1195, Aug. 1976, doi: 10.1007/BF02656602.
[23] C. J. McMahon, “Solute segregation and intergranular fracture in steels: a status report,” *Materials Science and Engineering*, vol. 42, pp. 215–226, Jan. 1980, doi: 10.1016/0025-5416(80)90031-2.
[24] X. Z. Zhang and J. F. Knott, “Cleavage fracture in bainitic and martensitic microstructures,” *Acta Materialia*, vol. 47, no. 12, pp. 3483–3495, Sep. 1999, doi: 10.1016/S1359-6454(99)00200-1.
[25] Z. Yang, Z. Liu, X. He, S. Qiao, and C. Xie, “Effect of microstructure on the impact toughness and temper embrittlement of SA508Gr.4N steel for advanced pressure vessel materials,” *Scientific Reports*, vol. 8, no. 1, p. 207, Dec. 2018, doi: 10.1038/s41598-017-18434-3.
[26] P. Bowen, S. G. Druce, and J. F. Knott, “Effects of microstructure on cleavage fracture in pressure vessel steel,” *Acta Metallurgica*, vol. 34, no. 6, pp. 1121–1131, Jun. 1986, doi: 10.1016/0001-6160(86)90222-1.
[27] R. Viswanathan and A. Joshi, “Effect of microstructure on the temper embrittlement of Cr-Mo-V steels,” *Metallurgical and Materials Transactions A*, vol. 6, no. 12, p. 2289, décembre 1975, doi: 10.1007/BF02818656.
[28] A. Akhatova *et al.*, “Investigation of the dependence of phosphorus segregation on grain boundary structure in Fe-P-C alloy: cross comparison between Atom Probe Tomography and Auger Electron Spectroscopy,” *Applied Surface Science*, vol. 463, pp. 203–210, Jan. 2019, doi: 10.1016/j.apsusc.2018.08.085.
[29] T. G. Lach *et al.*, “Correlative STEM-APT characterization of radiation-induced segregation and precipitation of in-service BWR 304 stainless steel,” *Journal of Nuclear Materials*, vol. 549, p. 152894, Jun. 2021, doi: 10.1016/j.jnucmat.2021.152894.
[30] L. Zhang, B. Radiguet, P. Todeschini, C. Domain, Y. Shen, and P. Pareige, “Investigation of solute segregation behavior using a correlative EBSD/TKD/APT methodology in a 16MND5 weld,” *Journal of Nuclear Materials*, vol. 523, pp. 434–443, Sep. 2019, doi: 10.1016/j.jnucmat.2019.06.002.
[31] V. J. Keast and D. B. Williams, “Grain boundary chemistry,” *Current Opinion in Solid State and Materials Science*, vol. 5, no. 1, pp. 23–30, Jan. 2001, doi: 10.1016/S1359-0286(00)00029-2.
[32] V. J. Keast and D. B. Williams, “Quantification of boundary segregation in the analytical electron microscope,” *J Microsc*, vol. 199, no. 1, pp. 45–55, Jul. 2000, doi: 10.1046/j.1365-2818.2000.00694.x.
[33] T. Walther, A. Rečnik, and N. Daneu, “A Novel Method of Analytical Transmission Electron Microscopy for Measuring Highly Accurately Segregation to Special Grain Boundaries or Planar Interfaces,” *Microchimica Acta*, vol. 155, no. 1–2, pp. 313–318, Sep. 2006, doi: 10.1007/s00604-006-0562-5.

[34] D. B. Williams, M. Watanabe, A. J. Papworth, and J. C. Li, “Quantitative characterization of the composition, thickness and orientation of thin films in the analytical electron microscope,” *Thin Solid Films*, vol. 424, no. 1, pp. 50–55, Jan. 2003, doi: 10.1016/S0040-6090(02)00906-9.
[35] J. A. S. Ikeda, Y.-M. Chiang, A. J. Garratt-Reed, and J. B. V. Sande, “Space Charge Segregation at Grain Boundaries in Titanium Dioxide: II, Model Experiments,” *Journal of the American Ceramic Society*, vol. 76, no. 10, pp. 2447–2459, 1993, doi: 10.1111/j.1151-2916.1993.tb03965.x.
[36] T. Hu, S. Yang, N. Zhou, Y. Zhang, and J. Luo, “Role of disordered bipolar complexions on the sulfur embrittlement of nickel general grain boundaries,” *Nature Communications*, vol. 9, no. 1, p. 2764, 17 2018, doi: 10.1038/s41467-018-05070-2.
[37] T. Walther *et al.*, “How to best measure atomic segregation to grain boundaries by analytical transmission electron microscopy,” *J Mater Sci*, p. 11, 2014.
[38] C.-Y. Hsu, J. Stodolna, P. Todeschini, F. Delabrouille, B. Radiguet, and F. Christien, “Accurate quantification of phosphorus intergranular segregation in iron by STEM-EDX,” *Micron*, vol. 153, p. 103175, Spring 2022, doi: 10.1016/j.micron.2021.103175.
[39] C.-Y. Hsu *et al.*, “Solute interface segregation measurement: Cross comparison between four different analytical methods,” *Applied Surface Science*, vol. 598, p. 153784, Oct. 2022, doi: 10.1016/j.apsusc.2022.153784.
[40] R. Viswanathan, “Temper embrittlement in a Ni-Cr steel containing phosphorus as impurity,” *Metall Mater Trans B*, vol. 2, no. 3, pp. 809–815, Mar. 1971, doi: 10.1007/BF02662740.
[41] S. Khan and M. A. Islam, “Influence of Prior Austenite Grain Size on the Degree of Temper Embrittlement in Cr-Mo Steel,” *Journal of Materials Engineering and Performance*, vol. 16, pp. 80–85, Feb. 2007, doi: 10.1007/s11665-006-9012-0.
[42] C. L. Briant and S. K. Banerji, “Intergranularfailure in steel: the role of grain-boundary composition,” *International Metals Reviews*, vol. 23, no. 1, pp. 164–199, Jan. 1978, doi: 10.1179/imtr.1978.23.1.164.
[43] M. Guttmann, “Thermochemical Interactions Versus Site Competition in Grain Boundary Segregation and Embrittlement in Multicomponent Systems,” *Le Journal de Physique IV*, vol. 05, no. C7, pp. C7-85-C7-96, Nov. 1995, doi: 10.1051/jp4:1995707.
[44] Ph. Dumoulin, M. Guttmann, M. Foucault, M. Palmier, M. Wayman, and M. Biscondi, “Role of molybdenum in phosphorus-induced temper embrittlement,” *Metal Science*, vol. 14, no. 1, pp. 1–15, Jan. 1980, doi: 10.1179/030634580790438163.
[45] Yu. I. Ustinovshikov, “Effects of alloying elements, impurities, and carbon on temper embrittlement of steels,” *Metal Science*, vol. 18, no. 12, pp. 545–548, Dec. 1984, doi: 10.1179/030634584790419683.
[46] C. J. McMahon, A. K. Cianelli, and H. C. Feng, “The influence of Mo on P-lnduced temper embrittlement in Ni-Cr steel,” *Metall Mater Trans A*, vol. 8, no. 7, pp. 1055–1057, Jul. 1977, doi: 10.1007/BF02667389.
[47] S. Suzuki, K. Abiko, and H. Kimura, “Phosphorus segregation related to the grain boundary structure in an Fe-P alloy,” *Scripta Metallurgica*, vol. 15, no. 10, pp. 1139–1143, Oct. 1981, doi: 10.1016/0036-9748(81)90175-7.
[48] T. Ogura, T. Masumoto, T. Watanabe, and S. Karashima, “Dependence of phosphorus segregation on grain boundary crystallography in an FeNiCr alloy,” *Acta Metallurgica*, vol. 35, no. 7, pp. 1807–1814, 1987.

[49] H. Kitahara, R. Ueji, N. Tsuji, and Y. Minamino, “Crystallographic features of lath martensite in low-carbon steel,” *Acta Materialia*, vol. 5, no. 54, pp. 1279–1288, 2006, doi: 10.1016/j.actamat.2005.11.001.
[50] S. Morito, X. Huang, T. Furuhara, T. Maki, and N. Hansen, “The morphology and crystallography of lath martensite in alloy steels,” *Acta Materialia*, vol. 54, no. 19, pp. 5323–5331, Nov. 2006, doi: 10.1016/j.actamat.2006.07.009.
[51] H. K. D. H. Bhadeshia, *Bainite in steels: theory and practice*, Third edition. Leeds, UK: Maney Publishing, 2015.
[52] H. I. Aaronson, W. T. Reynolds, G. J. Shiflet, and G. Spanos, “Bainite viewed three different ways,” *MTA*, vol. 21, no. 6, pp. 1343–1380, Jun. 1990, doi: 10.1007/BF02672557.
[53] B. L. Bramfitt and J. G. Speer, “A perspective on the morphology of bainite,” *MTA*, vol. 21, no. 3, pp. 817–829, Mar. 1990, doi: 10.1007/BF02656565.
[54] S. Zajac, V. Schwinn, and K. H. Tacke, “Characterisation and Quantification of Complex Bainitic Microstructures in High and Ultra-High Strength Linepipe Steels,” *MSF*, vol. 500–501, pp. 387–394, Nov. 2005, doi: 10.4028/www.scientific.net/MSF.500-501.387.
[55] G. Kurdjumow and G. Sachs, “Über den Mechanismus der Stahlhärtung,” *Zeitschrift fur Physik*, vol. 64, pp. 325–343, May 1930, doi: 10.1007/BF01397346.
[56] Gourgues A.-F., H. M. Flower, and T. C. Lindley, “Electron backscattering diffraction study of acicular ferrite, bainite, and martensite steel microstructures,” *Materials Science and Technology*, vol. 16, no. 1, pp. 26–40, Jan. 2000, doi: 10.1179/026708300773002636.
[57] P. Doig, D. Lonsdale, and P. E. J. Flewitt, “Segregation of embrittling elements to prior austenite grain boundaries in 2·25Cr–1 Mo steel,” *Metal Science*, vol. 16, no. 7, pp. 335–344, Jul. 1982, doi: 10.1179/030634582790427488.
[58] R. Chaouadi, J. Van Eyken, R. Gérard, M. Lambrecht, and I. Uytdenhouwen, “Effect of step cooling and P-segregation to grain boundaries on the tensile and fracture toughness properties of A533B plate and A508 forging steels,” *Journal of Nuclear Materials*, vol. 550, p. 152924, Jul. 2021, doi: 10.1016/j.jnucmat.2021.152924.
[59] S. Fladischer, “Applocation of new EDXS quantification schemes in TEM to organic semiconducting devices,” Graz University of Technology, 2013. [Online]. Available: https://diglib.tugraz.at/application-of-new-edxs-quantification-schemes-in-tem-to-organic-semiconducting-devices-2013
[60] G. Cliff and G. W. Lorimer, “The quantitative analysis of thin specimens,” *Journal of Microscopy*, vol. 103, no. 2, pp. 203–207, Mar. 1975, doi: 10.1111/j.1365-2818.1975.tb03895.x.
[61] P. J. Sheridan, “Determination of experimental and theoretical kASi factors for a 200-kV analytical electron microscope,” *Journal of Electron Microscopy Technique*, vol. 11, no. 1, pp. 41–61, Jan. 1989, doi: 10.1002/jemt.1060110107.
[62] J. Philibert, “A Method for Calculating the Absorption Correction in Electron-Probe Microanalysis,” in *X-ray Optics and X-ray Microanalysis*, Elsevier, 1963, pp. 379–392. doi: 10.1016/B978-1-4832-3322-2.50039-1.
[63] Y.-R. Im, B.-J. Lee, Y. J. Oh, J. H. Hong, and H.-C. Lee, “Effect of microstructure on the cleavage fracture strength of low carbon Mn–Ni–Mo bainitic steels,” *Journal of Nuclear Materials*, vol. 324, no. 1, pp. 33–40, Jan. 2004, doi: 10.1016/j.jnucmat.2003.09.003.
[64] Y.-R. Im, Y.-J. Oh, B.-J. Lee, J. H. Hong, and H.-C. Lee, “Effects of carbide precipitation on the strength and Charpy impact properties of low carbon Mn-Ni-Mo bainitic steels,” *Journal of Nuclear Materials - J NUCL MATER*, vol. 297, pp. 138–148, Aug. 2001, doi: 10.1016/S0022-3115(01)00610-9.

[65] S. Lee, S. Kim, B. Hwang, B. S. Lee, and C. G. Lee, “Effect of carbide distribution on the fracture toughness in the transition temperature region of an SA 508 steel,” *Acta Materialia*, vol. 50, no. 19, pp. 4755–4762, Nov. 2002, doi: 10.1016/S1359-6454(02)00313-0.
[66] T. Nyyssönen, M. Isakov, P. Peura, and V.-T. Kuokkala, “Iterative Determination of the Orientation Relationship Between Austenite and Martensite from a Large Amount of Grain Pair Misorientations,” *Metallurgical and Materials Transactions A*, vol. 47, 2016, doi: 10.1007/s11661-016-3462-2.
[67] F. Bachmann, R. Hielscher, and H. Schaeben, “Texture Analysis with MTEX–Free and Open Source Software Toolbox,” *Solid State Phenomena*, vol. 160, Feb. 2010, doi: 10.4028/www.scientific.net/SSP.160.63.
[68] H. Pous-Romero and H. K. D. H. Bhadeshia, “Continuous Cooling Transformations in Nuclear Pressure Vessel Steels,” *Metall and Mat Trans A*, vol. 45, no. 11, pp. 4897–4906, Oct. 2014, doi: 10.1007/s11661-014-2433-8.
[69] S. Cazottes *et al.*, “Quantitative microstructural characterization of nuclear grade bainitic steel: Influence of macrosegregations in full-scale forgings,” *Materials Characterization*, vol. 176, p. 111098, Jun. 2021, doi: 10.1016/j.matchar.2021.111098.
[70] C. Paré, C. Domain, J. Vidal, and C. Becquart, “Solute segregation at (100) and (110) tilt grain boundaries in Fe at the atomic scale,” presented at the Intergranular and interphase boundaries in materials, Paris, 2019.

8. Acknowledgement

The authors address special thanks to B. Marini who provided valuable insights during this work.